Fabrication of High-Quality Thin Solid-State Electrolyte Films Assisted by Machine Learning

Yu-Ting Chen,[▽] Marc Duquesnoy,[▽] Darren H. S. Tan, Jean-Marie Doux, Hedi Yang, Grayson Deysher, Phillip Ridley, Alejandro A. Franco,* Ying Shirley Meng,* and Zheng Chen*

ABSTRACT: Solid-state electrolytes (SSEs) are promising candidates to circumvent flammability concerns of liquid electrolytes. However, enhancing energy densities by thinning SSE layers and enabling scalable coating processes remain challenging. While previous studies have addressed thin and flexible SSEs, mainly ionic conductivity was considered for performance evaluation, and no systematic research on the effects of manufacturing conditions on the quality of SSE films was performed. Here, both uniformity and ionic conductivity are considered for evaluating the SSE films under the guidance of machine learning (ML). Three algorithms, principal component analysis, *K-means* clustering, and support vector machine, are employed to decipher the interdependencies between manufacturing conditions and film performance. Guided by ML, a 40 μm SSE film with high ionic conductivity and good uniformity is used to construct a $LiNi_{0.8}Co_{0.1}Mn_{0.1}O_2$ ‖ Li_6PS_5Cl ‖ LiIn cell demonstrating 100 cycles. This study presents an efficient ML-assisted approach to optimize scalable production of high-quality SSE films.

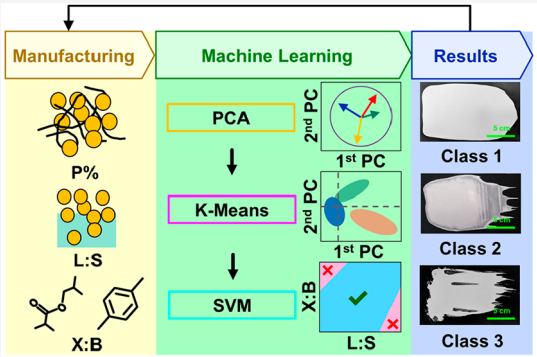

Li-ion batteries (LIBs) are currently the predominant energy storage technology widely used in portable electronic devices, electric vehicles, and grid energy storage.[1] Conventional LIBs employ liquid electrolytes containing flammable organic solvents, making them susceptible to leakage and potential flammability concerns.[2−5] One of the solutions to circumvent this is to replace liquid electrolytes with inorganic solid-state electrolytes (SSEs) in order to produce all-solid-state batteries (ASSBs) with improved safety and wider operating temperature ranges.[2,6] As a result, significant efforts have been devoted to developing various SSEs, some of which have exhibited ionic conductivities reaching 10^{-2} S cm^{-1} at room temperature, close to those of liquid electrolytes.[7−9] However, because of mechanical property limitations and under-developed manufacturing processes for inorganic SSEs, cells with pellet-type SSE layers thicker than 200 μm are still predominantly employed in ASSB research.[10] Unlike cathode and anode materials, electrolytes do not store energy, and thus, using thick SSE layer limits energy density.[2,11] To compete with conventional LIBs, it is therefore crucial to develop new fabrication processes that enable the manufacturing of cells using film-type SSE layers with reduced thicknesses, ideally 25−50 μm, to reach high energy density, while still maintaining ideal mechanical properties.[11] These fabrication techniques must also be compatible with existing manufacturing methods, such as conventional doctor-blade or roll-to-roll coating processes.

The most common way to address these aforementioned issues is to include polymer binders in the SSE composite, as they provide an added flexibility to the fabricated SSE films to compensate for mechanical weakness of pellet-type SSEs. Indeed, mechanical failures of SSEs in ASSBs are detrimental to battery performance.[2] This approach also enables a scalable doctor-blade or roll-to-roll solution process.[12] Film-type SSEs, combining sulfide inorganic SSEs with polymer binders and fabricated with doctor-blade, have been reported in the literature (Table 1) with ionic conductivities ranging between 10^{-5} and 10^{-3} S cm^{-1}. This wide conductivity variation can be attributed in part to the usage of different polymer binders and SSEs. However, even when similar polymer binders and

Table 1. Summary of Ionic Conductivity and Thickness of Recently Reported SSE Films Processed with Different Manufacturing Conditions[a]

electrolyte	binder	solvent	binder content	liquid: solid ratio	ionic conductivity (S cm^{-1})	thickness (μm)	ref
Li_6PS_5Cl	acrylate type	xylene: isobutyl isobutyrate (50:50)	1 wt %		1.3×10^{-3}	30	13
Li_3PS_4	SBS	anisole	3 wt %		2×10^{-4}	60	14
$Li_7P_3S_{11}$	SEBS	xylene	2.5 wt %	1	7×10^{-4}	55	15
Li_3PS_4	PEO	acetonitrile	5 wt %	4.6	8.4×10^{-6}	10	16
Li_6PS_5Cl	PEO	acetonitrile	5 wt %		2.0×10^{-4}	65	17
Li_3PS_4	NBR	xylene	3 wt %		4.2×10^{-4}		18
Li_3PS_4	NBR	THF	5.5 wt %		1.0×10^{-4}	70	19
Li_6PS_5Cl	NBR	xylene				30	20
Li_6PS_5Cl	poly(tert-butyl acrylate)-b-poly(1,4-butadiene)	isobutyl isobutyrate	2.5 wt %		1.7×10^{-3}	150	21
Li_6PS_5Cl	PBMA	xylene: isobutyl isobutyrate (0:100−100:0)	3%−10%	0.6−1.4	1.5×10^{-4}−8.6×10^{-4}	40	this work

[a]SBS, polystyrene-*block*-polybutadiene-*block*-polystyrene; SEBS, polystyrene-*block*-poly(ethylene-*ran*-butylene)-*block*-polystyrene); PEO, poly(ethylene oxide); NBR, nitrile butadiene rubber; PBMA, poly(butadiene methacrylate); THF, tetrahydrofuran.

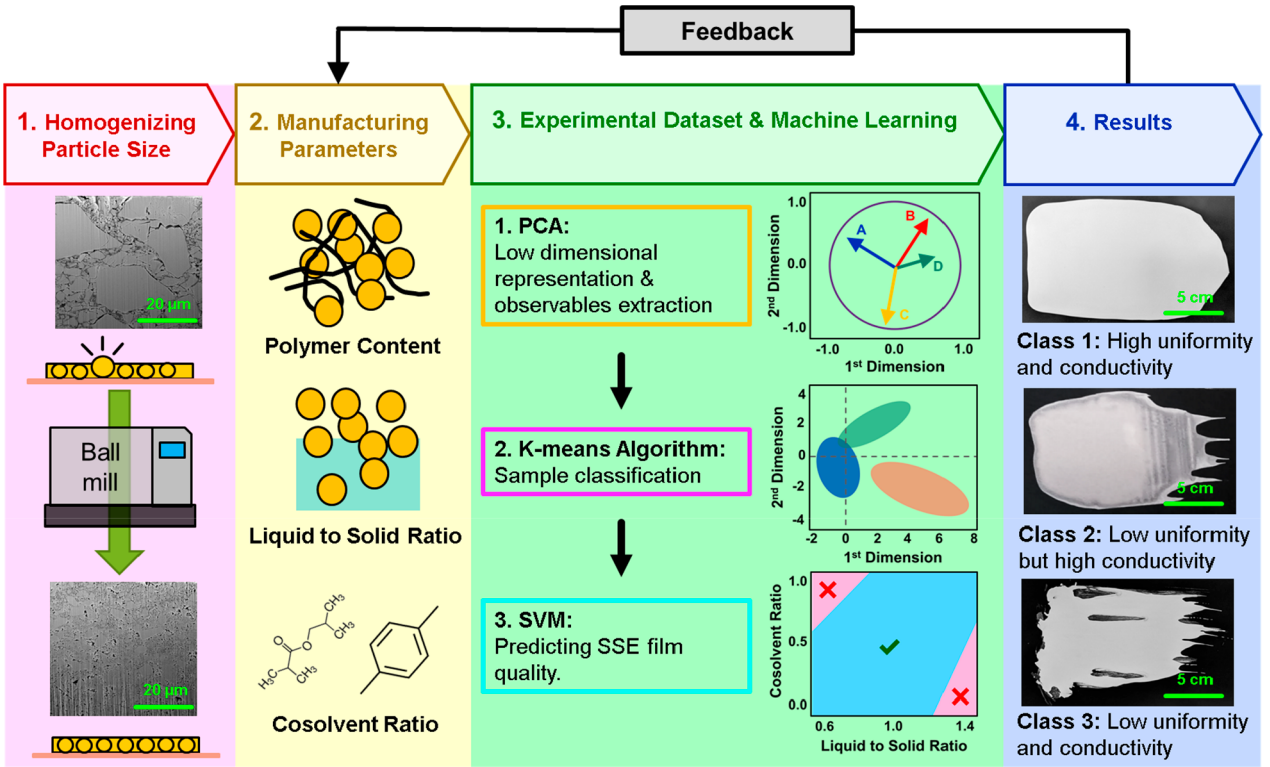

Figure 1. Schematic presenting the methodology developed in this work. First, ball-milling is used to reduce the particle size of the LPSCl electrolyte. Then, 110 slurries consisting of different polymer contents, liquid-to-solid ratios, and cosolvent ratios are fabricated to obtain the data set. This data set is fed into the machine learning workflow to categorize samples with different properties, as shown in the fourth step.

electrolytes were used, large variations in ionic conductivity can still be observed, indicating a high sensitivity to processing parameters (e.g., solvents, binder ratio, or liquid-to-solid ratio of the slurries) over the resulting ionic conductivity. Moreover, most reports limited evaluation of SSE films to mainly ionic conductivity, often ignoring the thickness uniformity of the produced film. Uniform and pinhole-free SSE layers are essential to electronically separate cathodes from anodes and to guide a uniform current and stress distribution, thus preventing short-circuit of ASSBs, which is one of the most important safety requirements for batteries. They are also crucial for maintaining consistent quality in mass production. Thus, a systematic study of the relationship between manufacturing conditions and the performance of SSE films is required.

Unfortunately, analyzing the correlations between multiple manufacturing parameters and performance metrics is challenging and requires intensive trial and error with conventional experimental methods.[22] Moreover, there may be nonlinear trends resulting from the synergistic effects of

different manufacturing parameters, making the multivariable puzzle even more complicated. Mesoscale physical simulations of the actual manufacturing process can offer deep insights on the mechanism of how manufacturing parameters impact the properties of SSE films,[23−26] but they are considered computationally expensive for high-throughput use with current hardware capabilities.[27] Machine learning (ML), with its proficiency in analyzing complex data sets with a large number of variables,[22,28−32] provides a new pathway to limit time-consuming trial and error processes. Moreover, ML, in combination with statistical methods, allows fast interpretation of data. In fact, ML has already been utilized in the battery field, either in estimating the state of charge or cycle life of cells under operation,[31,33] as well as to assist in the manufacturing process of LIB electrodes.[22,27] However, the application of ML to manufacturing flexible SSE films remains unexplored, presenting an opportunity to apply such capabilities to improve performance and overall quality of SSE films used in ASSBs.

This work seeks to predict the quality of SSE films by analyzing the multivariable interdependencies between performance and manufacturing parameters. The methodology used in this work is schematically presented in Figure 1. Before casting, Li_6PS_5Cl (LPSCl) powder, a commonly used inorganic Li^+ conductor, is wet-milled to homogenize its particle size and keeps it approximately 1 order of magnitude smaller than the target thickness of SSE films, preventing it from negatively affecting their uniformity. Of the multiple input parameters that need to be considered for performance evaluation, polymer content (P%), liquid-to-solid ratio (L:S), and cosolvent ratio (X:B) are chosen as the manufacturing parameters because they have a significant influence over the rheological properties of SSE slurries. After casting the SSE films, several output parameters [density (ρ), ohmic resistance (Ω), normalized conductivity (σ_i^N), deviation of thickness (DoT; the standard deviation of thickness measured over 9 different points on the SSE films), and relative thickness deviation (RD; the relative standard deviation of thickness, DoT/thickness)] are obtained. The obtained experimental data set, consisting of 110 slurry compositions, is used to perform a principal component analysis (PCA) to determine the most representative observables for performance metrics and manufacturing conditions.[34] Following PCA, the manufacturing conditions are classified according to a *K-means* clustering in order to define the quality of the SSE film in terms of σ_i^N, DoT, and RD. Afterward, hyperplanes are assigned using support vector machine (SVM) for a graphical visualization of specific effects.[35,36] This common thread aims to both present groups of manufacturing conditions with similar performances and find the effect of each manufacturing parameter on SSE films. Finally, an SSE film, with manufacturing conditions guided by the ML study, is applied to a NCM811 || LPSCl || LiIn cell to demonstrate the viability of this approach.

As broad particle size distributions of the SSE will adversely affect the uniformity of the SSE films, sizes need to be reduced to around 1 order of magnitude smaller than the target thickness of the films. This ensures consistency and allows for better film uniformity. As shown in Figure S1a, the pristine LPSCl powder exhibits a nonuniform particle size distribution with particles larger than 20 μm. Hence, reducing the particle size of the pristine powder is necessary. After dry ball-milling, some of the particles remain larger than 15 μm, suggesting that the process is not effective enough (Figure S1b). To overcome this, inert solvents are employed in wet ball-milling to prevent the aggregation of the particles and thus allow for reduced particle size. No particles larger than 10 μm are observed after wet ball-milling, as seen in Figure S1c−f. When the milling speed is increased to 400 and 500 rpm, the primary particle size can be further reduced, but simultaneously the ionic conductivity of the electrolyte powder decreases significantly. To avoid severe ionic conductivity loss, the milling speed is limited to 300 rpm, with an optimized milling time of 2 h. Under these milling conditions, the particle size is also further reduced while still preserving the ionic conductivity of the powder. As a result, all the electrolyte powders used for this study are processed using these wet ball-milling conditions. To evaluate the impact of ball-milling on the electrolyte's crystal structure, X-ray diffraction (XRD) patterns of the LPSCl powder are collected before and after various ball-milling procedures (Figure S2a). The positions of all Bragg peaks remain unchanged after ball-milling, indicating that the original LPSCl crystal structure is preserved. However, the samples can be distinguished by different extents of peak broadening (Figure S2b), indicating reduction in crystallinity after ball-milling. The peak broadening with increased milling speed is in good agreement with the lower conductivity measured by electrochemical impedance spectroscopy (EIS) presented in Figure S2c.

To reaffirm the importance of controlling SSE particle size, SSE films are fabricated using pristine and ball-milled LPSCl powder, and their focused-ion-beam (FIB) cross-section images are presented in Figure S3. When pristine LPSCl powder is employed, the film exhibits particles larger than 20 μm and is susceptible to crack formation during calendering. This can increase the risk of short circuit when the SSE films are used in ASSBs. In contrast, a more homogeneous film is obtained when employing ball-milled LPSCl, and no cracks are observed in the cross-sectional image. Thus, the ball-milled electrolyte powder is used for the collection of the data set necessary for the ML study.

To perform the doctor-blade process for LPSCl, solvents with good chemical compatibility with sulfide-based SSEs must be selected; namely, nonpolar solvents with high dielectric constant are required.[15] Moreover, suitable vapor pressures (at room temperature: xylene, 10 mmHg; isobutyl isobutyrate, 5 mmHg) and boiling points (xylene, 138 °C; isobutyl isobutyrate, 147 °C) are also essential for obtaining an optimum drying rate, which significantly influences the quality of SSE films. Thus, *p*-xylene and isobutyl isobutyrate are employed in conjunction for the LPSCl slurry preparation. To evaluate their chemical compatibility with the SSE, LPSCl powder is immersed into each of these solvents and no significant change is observed in both XRD patterns and ionic conductivities after drying (Figure S4), indicating that LPSCl does not degrade in either of these solvents.

The full experimental data set is presented in Table S1. After this training data set is collected, ML algorithms are used to analyze the effect of the polymer content (P%), the liquid-to-solid ratio (L:S; volume of solvent/weight of LPSCl, in μL/mg), and the cosolvent ratio (X:B; xylene to isobutyl isobutyrate ratio, represented by the volumetric percentage of xylene) on the quality of the SSE films. After casting, ρ, Ω, σ_i^N, DoT, and RD are measured. Because eight different variables are experimentally generated, a PCA[34] is conducted to project manufacturing conditions in a reduced dimensional subspace for reflecting (i) interdependencies between variables

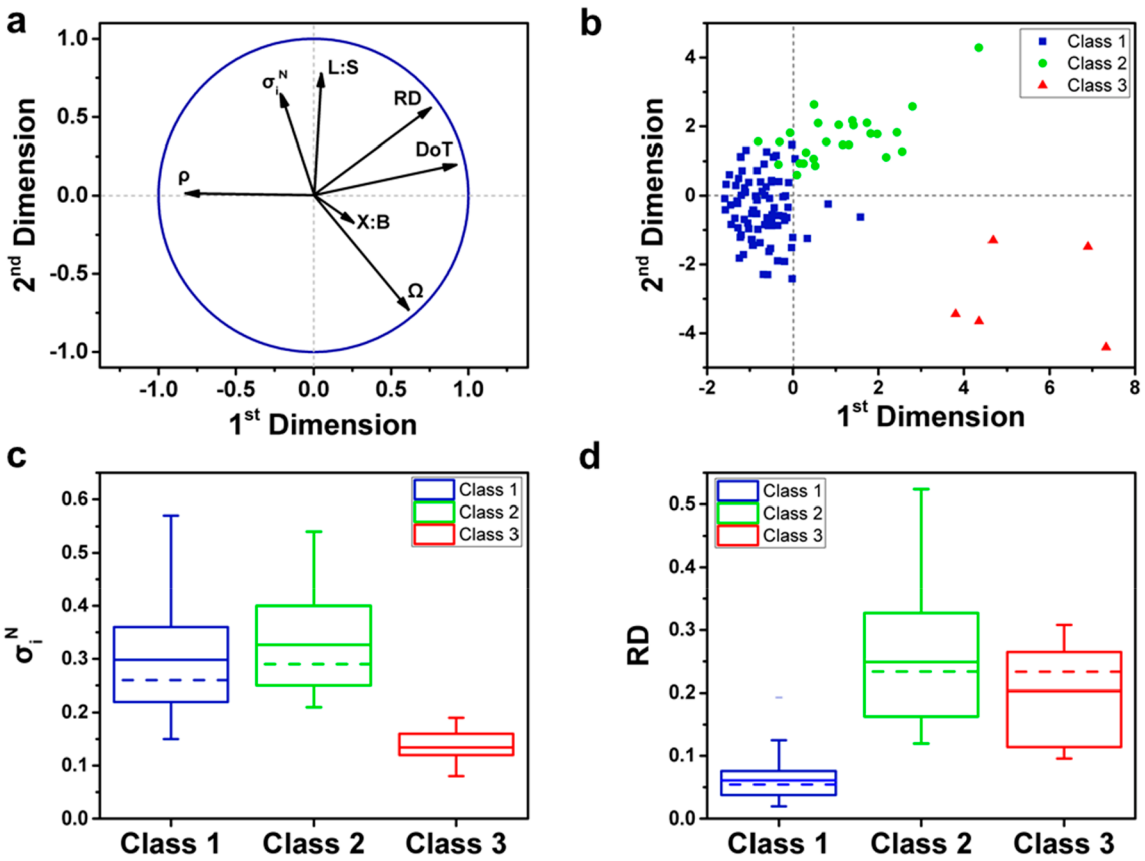

Figure 2. Data analysis results coming from the implementation of the PCA and the *K-means* algorithm which show the linear dependence between initial variables and the grouping of the samples in terms of performance respectively. (a) Projection of the initial variables (symbolized by black arrows) onto the 2D plan formed by the first two principal components resulting from the PCA implementation, with the purpose to visualize and analyze the correlation between each pair of variables. For the PCA implementation, P% is not taken into account because of a low number of different modalities. It is considered as a qualitative variable and did not appear in the initial PCA features for better results. However, P% is used for the rest of the analysis. (b) All samples are grouped into 3 clusters with the *K-means* algorithm, here represented within the two first principal components. Those clusters are explicitly defined as *classes* in the rest of the study. Box charts for the comparison of distribution of (c) normalized conductivity and (d) relative thickness deviation for all 3 classes. Abbreviations: L:S, liquid-to-solid ratio; X:B, cosolvent ratio; ρ, density; Ω, ohmic resistance; σ_i^N, normalized conductivity; DoT, deviation of thickness; RD, relative thickness deviation.

and (ii) the spread of manufacturing conditions along new principal components. Indeed, such data compression is based on a search for directions of maximum variance to build a new subspace with fewer dimensions, in which the initial raw data are projected. The resulting principal components are a linear combination of initial variables that are orthogonal to each other. This PCA implementation aims at selecting a subset of principal components that can reflect the variance of the experimental data set to define the relationship between manufacturing conditions and film quality.

The correlations between the initial variables can be visualized by projecting them onto two-dimensional subspace, and the result is presented in Figure 2a. As expected, the PCA shows that σ_i^N is inversely correlated with resistance (eq 1 in the Supporting Information). However, it appears that while DoT and RD are strongly correlated together, they are not linearly correlated with σ_i^N. As a result, σ_i^N (corresponding to the ionic conductivity of the film) and RD (representing the film uniformity) are employed to evaluate performances of the SSE films. The independence between σ_i^N and RD highlights the shortcomings of evaluating SSE films solely based on ionic conductivities alone, as commonly done in the literature.[13−21] Based on the PCA analysis, it is conceivable that highly conductive films might be perceived as being of high quality, while they exhibit large RDs that result in poor cell performance during electrochemical testing.

To visualize the interdependencies among manufacturing conditions and performance, thickness, DoT, and σ_i^N are plotted as a function of L:S and X:B for different P%. The results are presented in Movies S1, S2, and S3, respectively. As P% increases, the overall thickness also increases, while σ_i^N decreases. This may be a result of higher slurry viscosities that limit the flow along the surface of the substrate. Higher P% also increases the tortuosity factor of Li^+ electromigration, resulting in poorer bulk σ_i^N compared to bare LPSCl.[12] The thickness increases drastically when high X:B, low L:S, and P% larger than 5% are used. With these manufacturing conditions, slurries become too viscous, causing the LPSCl powder to aggregate. While trends in ionic conductivity are relatively intuitive, the plots for DoT exhibit a complex nonlinear behavior. The region with low deviation shifts dramatically as the P% changes. To obtain a better overview, DoT values are averaged over the four P% and plotted in Figure 3. The region with low deviation is found to be distributed in a counter-

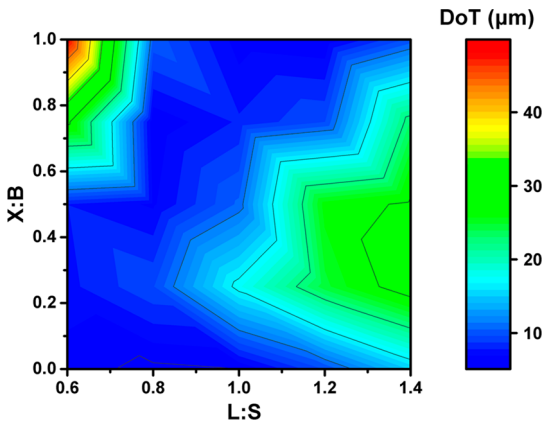

Figure 3. DoT vs L:S and X:B contour plot averaging through P% of 3%, 5%, 7%, and 10%.

intuitive way. This implies that it is challenging to deconvolute the interdependencies among manufacturing conditions and performance using simple statistical methods. Hence, clustering analysis is employed in the next step.

Before explicitly looking at the effect of manufacturing conditions, it is useful to create groups with similar characteristics in terms of performance, namely, σ_i^N and RD from the PCA results. The *K-means* algorithm is directly applied on principal components, and the results are presented in Figure 2b.[35] The purpose of the algorithm is to obtain clusters of manufacturing conditions represented by centroids in the low dimensional subspace with the same characteristics in terms of performances, without any prior information (patterns of manufacturing values) on the obtained labels. In order to separate the data, *K-means* algorithm finds patterns where manufacturing conditions inside clusters are similar. The algorithm finds in total 3 different clusters. For the rest of the study, a cluster of manufacturing conditions is called a *class* in order to characterize properly a type of SSE films. The apparent interception of the boundaries from class 1 and class 2 is due to the projection onto a 2D space, whereas the clustering algorithm is applied to more than two principal components. These classes are well-separated from each other by other dimensions before projecting on the 2D space. The statistics of σ_i^N and RD in all classes are presented in Figure 2c,d, where a nonparametric *Kruskal–Wallis* test is applied to statistically compare the distributions of σ_i^N and RD between classes.[37] This test is relevant to compare more than two samples, assume that residuals of the tests are not following a normal distribution, and conclude on possible significant differences between medians of distributions. In that sense, it will validate the *K-means* clustering in order to discriminate SSE films based on their properties. For the test itself, the *p*-value, generally written as "*p*", represents the probability to reject the hypothesis of the differences in distributions. As a consequence, the test presents significant differences ($p \leq 0.05$) of distribution among the classes in this study.[37] It appears that both class 1 and class 2 exhibit a high ionic conductivity σ_i^N compared to class 3. Class 1 can be further separated from class 2 as it exhibits the lowest RD (i.e., higher film uniformity). To conclude, class 1 exhibits good σ_i^N and low RD; class 2 maintains the good σ_i^N from class 1 while exhibiting an increased RD; class 3 shows the worst performance in terms of both σ_i^N and RD. As a consequence, the classification of the overall performance of SSE films can be defined by common characteristics of observables within each class.

It is also worth looking at the manufacturing condition's relationships with different classes. As the polymer is insulative compared to LPSCl, the ionic conductivity decreases as the P% increases. As expected, the average P% in class 3 is higher than that of classs 1 and 2. Nevertheless, no statistical effect is found for P% on RD. When looking at L:S, one may conclude that employing higher L:S facilitates higher σ_i^N according to the PCA result. Indeed, the classes with higher conductivity contain higher ranges of L:S. However, to minimize the RD, the ratio must be kept in an intermediate range, namely, 0.92 ± 0.23, which is the average value within class 1. Class 3 appears to have the highest X:B, implying a possible adverse effect of X:B over performance. However, an Anova calculation (with a logarithmic correction on the dependent variable)[38] indicates that X:B and L:S have synergistic effects on RD. Although qualitative conclusions can be drawn after conducting the *K-means* algorithm, the link between manufacturing conditions and performance remains obscure because of the synergistic effect among different variables. Thus, numeric relationships between manufacturing conditions and performance need to be deciphered before the ML model can gain the ability to predict the results.

While the manufacturing conditions–performance relationship appears clearer after *K-means* clustering, it needs to be further deconvoluted through SVM.[36] Such a powerful and widely used classification learning technique optimizes the separation of classes from each other by constructing a linear hyperplane in the low-dimensional subspace defined above, to maximize the margin between different classes (Figure S5). Therefore, the margin is defined as the distance between the separating hyperplane (also called decision boundary) and training raw data. The larger the margin, the better the classification prediction. Consequently, the separation of classes and the decision boundaries are interesting as a visualization tool of the results. Indeed, it is possible to fix one manufacturing parameter and display the classification results as well as the decision boundary in a 2D plot formed by ranges of the two other parameters. In that sense, it is possible to analyze the evolution of the boundary when manufacturing conditions change, which reflects their impact on the performance.[22]

This process allows the prediction of film performance associated with a specific set of manufacturing conditions. To train the SVM model, 80% of the total number of raw data are randomly selected as the training data set, and the remaining data are used as the testing data set to validate the model. To overcome the unbalanced class distribution, a random oversampling procedure method is applied on the training dataset to fix the class imbalance (Figure S6) by adjusting class distribution over the minority classes (i.e., class 2 and 3).[39] Such a random oversampling approach allows the SVM algorithm to learn data distribution in equal proportions of samples per class, whereas unbalanced numbers of samples would cause SVM to yield inaccurate results by prioritizing the class with the largest number of samples. In other words, the metric used to validate the model considers the weighted training of the SVM algorithm by providing a better value when predicting manufacturing conditions as a minor class.

The best linear hyperplane is assigned by SVM to divide the low dimensional subspace spanned by the 1st and 2nd principal components into three regions. The results based on σ_i^N and

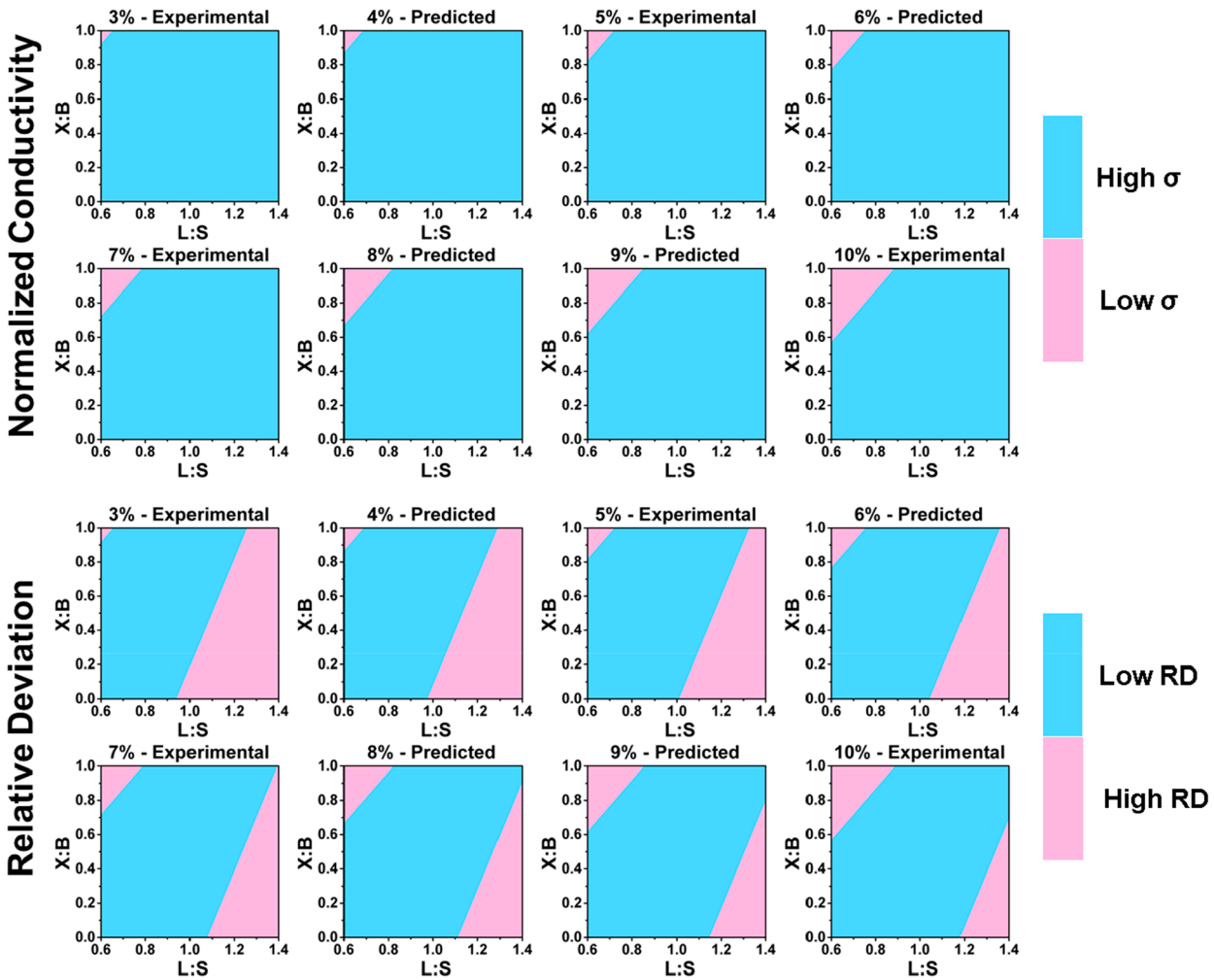

Figure 4. SVM classification in terms of the ionic conductivity (σ_i^N) and the relative thickness deviation (RD) of SSE films as a function of L:S and X:B ratios. The manufacturing conditions with P% of 3%, 5%, 7%, and 10% are obtained through experiment, while 4%, 6%, 8%, and 9% are interpolated using the ML model.

RD are presented in Figure 4. When accounting only for σ_i^N as the performance metric, most of the manufacturing conditions are considered to result in good film quality. However, when considering the RD as well, a large portion of manufacturing conditions, with mid-to-high L:S are no longer qualified so. Therefore, the three regions, from low L:S to high L:S, can be related to class 3, class 1, and class 2, respectively. Besides the data points obtained through experiment, SVM is also able to predict using new manufacturing conditions, interpolating the results with P% of 4%, 6%, 8%, and 9%. When projected on the L:S–X:B plane, the hyperplane appears to be sloped and will shift as P% changes, showing the counterintuitive trend caused by the high interdependency of each manufacturing parameter. When comparing the trends found in Figure 4 with the interpretations of *K-means* clustering and the statistical tests, they match in terms of the effects of manufacturing parameters, indicating that the ML classifier is suitable for analyzing interdependencies between manufacturing parameters and quality of SSE films. The model is validated with the testing data set through the F1-score metric[40] that reaches a value of 94%. Such a metric is relevant for multilabel classification learning because it helps to balance the metric across the sensitivity and the specificity of the model. The F1-score is an average definition of precision and recall, and an example of a binary classification task is shown below:

$$\mathrm{F1} = 2 \times \frac{\mathrm{precision} \times \mathrm{recall}}{\mathrm{precision} + \mathrm{recall}} \tag{1}$$

$$\mathrm{precision} = \frac{\mathrm{RP}}{\mathrm{RP} + \mathrm{FP}} \tag{2}$$

$$\mathrm{recall} = \frac{\mathrm{RP}}{\mathrm{RP} + \mathrm{FN}} \tag{3}$$

where RP, FP, and FN are the true predicted values, the mis-predicted false values, and the mis-predicted true values, respectively. The true/false prediction is defined as a manufacturing condition correctly/wrongly classified by the algorithm over the positive/negative value of the output. In the case of the multilabel classification developed in this study, the F1-score is averaged over the values between each pairs of labels for the output of the classification task. Because of the definition of three classes of film quality, it is possible to distinguish good and bad SSE films with respect to each performance variable.

To probe the connection between performance and morphologies of the SSE films, one sample is selected from

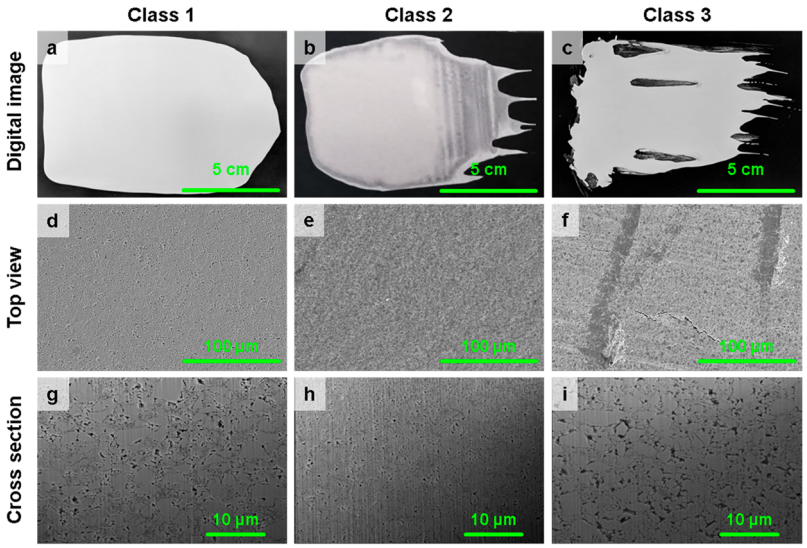

Figure 5. Images of representative SSE films from each class. (a−c) Digital images, (d−f) SEM top view, and (g−i) FIB cross-sectional views of the SSE films from (a, d, and g) class 1, (b, e, and h) class 2, and (c, f, and i) class 3.

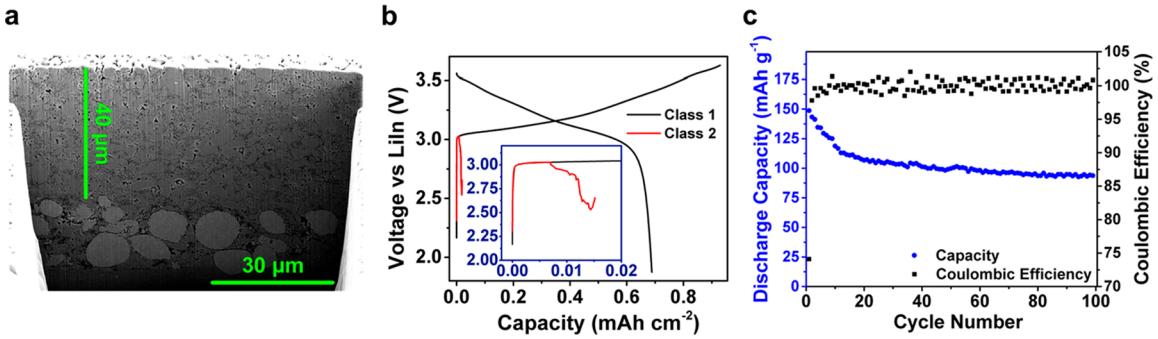

Figure 6. SEM cross-sectional image, first-cycle voltage profiles capacity retention and Coulombic efficiency of NCM811 || LPSCl || LiIn cells with a cathode loading of 4.75 mg cm^{-2}. (a) SEM cross-sectional image indicating that an intimate contact is formed between the electrolyte and the cathode composite. The measured thickness of the SSE film is 40 μm. (b) First cycle voltage profiles of NCM811 || LPSCl || LiIn cells prepared using SSE films from class 1 and class 2. Because of lower uniformity, the cell using the class 2 film shorts during the first cycle. (c) Capacity retention and Coulombic efficiency of the class 1 cell.

each class and their morphology observed using digital and scanning electron microscopy (SEM) images, as presented in Figure 5. From the digital images (Figure 5a−c), class 1 appears to be the most uniform and exhibits a clear-cut boundary with its substrate. Compared to class 1, class 2 exhibits inferior uniformity with a fading boundary to the substrate, likely because of the higher L:S in its manufacturing conditions. Severe aggregations can be observed in class 3 where the solvents fail to properly disperse the LPSCl powder because of insufficient L:S. When looking at the SEM top-down view images (Figure 5d−f), both class 1 and class 2 show uniform surface morphology, with class 1 appearing to be slightly superior. On the other hand, aggregated particles and cracks can be observed on the surface of the class 3 sample. FIB cross sections (Figure 5g−i) are collected to probe the interior morphology of the films. The particle distributions of classes 1 and 3 are similar, with class 3 being more porous. Class 2 exhibits smaller overall particle size, especially on the top part of the image, likely because of phase separation between the smaller and larger particles resulting from excessive L:S. To verify this assumption, another cross section is taken from the bottom side (Figure S7), and it appears that the average particle size is comparable to that of classes 1 and 3. Nevertheless, the overall porosity of class 2 is lower than that of class 1, probably because of the close packing of LPSCl particles facilitated by higher L:S, explaining the slightly higher σ_i^N in class 2 than class 1. Even though class 2 exhibits a dense cross-sectional morphology, its tendency to phase separate is not desirable for maintaining consistent quality in mass production. To prove its superior quality over the other two classes, a uniform free-standing SSE film from class 1 is fabricated and tested (Figure S8).

Before the application of SSE films to batteries, it is important to evaluate their electronic conductivity. An SSE with sufficient electronic insulation, preferably below the order of 10^{-9} S cm^{-1}, will prevent charge leakage or even short circuiting of the cells.[41,42] DC polarization and EIS results of the LPSCl powder and film are presented in Figure S9. While the pristine LPSCl powder exhibits an ionic conductivity of 2.1 $\times 10^{-3}$ S cm^{-1} and an electronic conductivity of 5.1 $\times 10^{-9}$ S cm^{-1}, the optimized LPSCl film has an ionic conductivity of 8.6 $\times 10^{-4}$ S cm^{-1} and an electronic conductivity of 1.1 $\times 10^{-9}$ S cm^{-1}. For both samples, the electronic conductivities are six orders smaller than their ionic conductivity. It is worth noting that although the LPSCl film exhibits a lower ionic conductivity than its powder form, the ability to be fabricated

with reduced thicknesses leads to a lower total impedance, as can be seen in Figure S9b. The fabrication of SSE films therefore not only is beneficial to energy density of the battery but also reduces ohmic losses during cycling.

SSE films from class 1 and 2 are used to prepare NCM811 || LPSCl || LiIn cells. An FIB cross-sectional image showing the SSE and the cathode layers after calendering is presented in Figure 6a. The whole cross section is observed to be uniform and dense. The cathode composite−SSE layer contact is also observed to be compliant, with no delamination, voids, or cracks observed. Their voltage profiles are presented in Figure 6b. When the class 1 film is employed, the cell cycles as expected, while a short circuit is observed during the first charge with the class 2 film. Nonuniform thickness of SSE films can cause uneven stress distribution during calendering and impact negatively on the integrity of the cell structure, leading to short circuit during the first charge. This illustrates the importance of considering both the uniformity and ionic conductivity of the SSE films for performance evaluation. Figure 6c shows the capacity retention and Coulombic efficiency (CE) of the NCM811 || LPSCl || LiIn cell made with the class 1 film. A first cycle CE of 74.1% along with a first discharge capacity of 149 mAh g^{-1} is obtained. The initial capacity loss in the first 10 cycles can be attributed to kinetic effects of contact losses and initial impedance growth at the cathode, which is commonly observed in the interfaces between sulfide SSEs and layered-oxide cathodes.[43,44] Variation in CE can be observed, and these may be attributed to the ionic conductivity change of SSE resulting from the slight fluctuation of room temperature. A capacity of 94 mAh g^{-1} is retained after 100 cycles. Another NCM811 || LPSCl || graphite cell with a cathode areal loading of 10 mg cm^{-2} was fabricated, and its voltage profiles and EIS are presented in Figure S10. The cell delivered a first discharge capacity of 1.61 mAh cm^{-2} and a first CE of 76.2%. The cell maintained stable charge−discharge cycling during the following cycles. This result further demonstrates the possibility of utilizing the ML approach in practical applications. Nevertheless, similar to the NCM811 || LPSCl || LiIn cell, the NCM811 || LPSCl || graphite cell also exhibits some contact losses at the cathode side, and its EIS slightly increases from 142 to 178 Ω after the first cycle. Future work will be focused on optimizing the cycling pressure of film-type ASSBs to mitigate the capacity loss caused by the volume change of layered-oxide cathode materials[43−45] and to increase the energy density by enabling Li-metal anodes.[46−49]

In summary, this study demonstrates how ML algorithms can be used to predict the performance of the sulfide-based SSE films by deconvoluting the interdependencies between the manufacturing parameters and performance metrics. After collection of the experimental data set, three algorithms (PCA, *K-means* algorithm, and SVM) in combination with statistical tests are employed to analyze the data. PCA determines the most significant observables for performance evaluation and allows to represent the manufacturing conditions in a low dimensional subspace. A clustering method, the *K-means* algorithm, is then applied in this subspace to properly define classes of films quality based on the similarity of performance within groups. These 3 classes are defined as class 1 (high σ_i^N and low RD), class 2 (high σ_i^N and high RD), and class 3 (low σ_i^N and high RD). Finally, the SVM model reveals the trends of the effect of the manufacturing parameters on the quality of SSE films according to classes, and supports the results found in the *K-means* clustering and statistical analysis. Finally, guided by ML, a NCM811 || LPSCl || LiIn cell, utilizing an SSE film with a thickness of 40 μm from class 1, is shown to be able to cycle successfully for 100 cycles. Our results highlight the necessity to account for both uniformity and ionic conductivity when fabricating SSE films and demonstrate how ML can be a powerful tool to guide experiments toward the optimal fabrication parameters. The methodology provided in this study may benefit the development of future scalable manufacturing process for flexible and uniform SSE films for ASSB applications.

■ ASSOCIATED CONTENT

Supporting Information

The Supporting Information is available free of charge at https://pubs.acs.org/doi/10.1021/acsenergylett.1c00332.

Experimental and machine algorithm details; SEM images, a digital image, XRD patterns, EIS data, and DC polarization of LPSCl powder or SSE films; DoT vs L:S and X:B plot; number of samples in each class (PDF)

Table S1: Full experimental data set (XLSX)

Movie S1: Visualization of the thickness as a function of L:S and X:B for different P% (MPG)

Movie S2: Visualization of the DoT as a function of L:S and X:B for different P% (MPG)

Movie S3: Visualization of σ_i^N as a function of L:S and X:B for different P% (MPG)

■ AUTHOR INFORMATION

Corresponding Authors

Alejandro A. Franco − *Laboratoire de Réactivité et Chimie des Solides (LRCS), Université de Picardie Jules Verne, UMR CNRS 7314, 80039 Amiens, France; Réseau sur le Stockage Electrochimique de l'Energie (RS2E), FR CNRS 3459, 80039 Amiens, France; Alistore-ERI European Research Institute, FR CNRS 3104, 80039 Amiens, France; Institut Universitaire de France, 75005 Paris, France*; Email: alejandro.franco@u-picardie.fr

Ying Shirley Meng − *Program of Materials Science and Engineering, Department of NanoEngineering, and Sustainable Power & Energy Center (SPEC), University of California San Diego, California 92093, United States;* orcid.org/0000-0001-8936-8845; Email: shmeng@ucsd.edu

Zheng Chen − *Program of Materials Science and Engineering, Department of NanoEngineering, Sustainable Power & Energy Center (SPEC), and Program of Chemical Engineering, University of California San Diego, California 92093, United States;* orcid.org/0000-0002-9186-4298; Email: zhengchen@eng.ucsd.edu

Authors

Yu-Ting Chen − *Program of Materials Science and Engineering, University of California San Diego, California 92093, United States;* orcid.org/0000-0001-9525-8407

Marc Duquesnoy − *Laboratoire de Réactivité et Chimie des Solides (LRCS), Université de Picardie Jules Verne, UMR CNRS 7314, 80039 Amiens, France; Réseau sur le Stockage Electrochimique de l'Energie (RS2E), FR CNRS 3459, 80039 Amiens, France; Alistore-ERI European Research Institute, FR CNRS 3104, 80039 Amiens, France*

Darren H. S. Tan − *Department of NanoEngineering, University of California San Diego, California 92093, United States*
Jean-Marie Doux − *Department of NanoEngineering, University of California San Diego, California 92093, United States*
Hedi Yang − *Department of NanoEngineering, University of California San Diego, California 92093, United States*
Grayson Deysher − *Program of Materials Science and Engineering, University of California San Diego, California 92093, United States;* orcid.org/0000-0003-0482-8991
Phillip Ridley − *Department of NanoEngineering, University of California San Diego, California 92093, United States*

Complete contact information is available at:
https://pubs.acs.org/10.1021/acsenergylett.1c00332

Author Contributions

[▽]Y.-T.C. and M.D. contributed equally to this work.

Notes

The authors declare no competing financial interest.

■ ACKNOWLEDGMENTS

This work was partially supported by LG Chem through the Battery Innovation Contest (BIC) program as well as the Energy & Biosciences Institute through the EBI-Shell program. Z.C. acknowledges funding from the start-up fund support from the Jacob School of Engineering at University of California San Diego. Y.S.M. acknowledges funding support from Zable Endowed Chair Fund. Part of this work was performed at the San Diego Nanotechnology Infrastructure (SDNI) of the UCSD, a member of the National Nanotechnology Coordinated Infrastructure, supported by the National Science Foundation (Grant ECCS-1542148). M.D. and A.A.F. acknowledge the European Union's Horizon 2020 research and innovation programme for the funding support through the European Research Council (Grant Agreement 772873, "ARTISTIC" project). M.D. and A.A.F. acknowledge the ALISTORE European Research Institute for funding support. A.A.F. acknowledges the Institut Universitaire de France for the support.

■ REFERENCES

(1) Chen, T.; Jin, Y.; Lv, H.; Yang, A.; Liu, M.; Chen, B.; Xie, Y.; Chen, Q. Applications of lithium-ion batteries in grid-scale energy storage systems. *Trans. Tianjin Univ.* **2020**, *26* (3), 208−217.
(2) Horowitz, Y.; Schmidt, C.; Yoon, D.-h.; Riegger, L. M.; Katzenmeier, L.; Bosch, G. M.; Noked, M.; Ein-Eli, Y.; Janek, J.; Zeier, W. G.; et al. Between Liquid and All Solid: A Prospect on Electrolyte Future in Lithium-Ion Batteries for Electric Vehicles. *Energy Technol.* **2020**, *8* (11), 2000580.
(3) Jung, Y. S.; Oh, D. Y.; Nam, Y. J.; Park, K. H. Issues and challenges for bulk-type all-solid-state rechargeable lithium batteries using sulfide solid electrolytes. *Isr. J. Chem.* **2015**, *55* (5), 472−485.
(4) Kerman, K.; Luntz, A.; Viswanathan, V.; Chiang, Y.-M.; Chen, Z. practical challenges hindering the development of solid state Li ion batteries. *J. Electrochem. Soc.* **2017**, *164* (7), A1731.
(5) Lee, H.; Oh, P.; Kim, J.; Cha, H.; Chae, S.; Lee, S.; Cho, J. Advances and Prospects of Sulfide All-Solid-State Lithium Batteries via One-to-One Comparison with Conventional Liquid Lithium Ion Batteries. *Adv. Mater.* **2019**, *31* (29), 1900376.
(6) Zhang, Q.; Cao, D.; Ma, Y.; Natan, A.; Aurora, P.; Zhu, H. Sulfide-based solid-state electrolytes: synthesis, stability, and potential for all-solid-state batteries. *Adv. Mater.* **2019**, *31* (44), 1901131.
(7) Seino, Y.; Ota, T.; Takada, K.; Hayashi, A.; Tatsumisago, M. A sulphide lithium super ion conductor is superior to liquid ion conductors for use in rechargeable batteries. *Energy Environ. Sci.* **2014**, *7* (2), 627−631.
(8) Kamaya, N.; Homma, K.; Yamakawa, Y.; Hirayama, M.; Kanno, R.; Yonemura, M.; Kamiyama, T.; Kato, Y.; Hama, S.; Kawamoto, K.; et al. A lithium superionic conductor. *Nat. Mater.* **2011**, *10* (9), 682.
(9) Janek, J.; Zeier, W. G. A solid future for battery development. *Nat. Energy* **2016**, *1* (9), 16141.
(10) Balaish, M.; Gonzalez-Rosillo, J. C.; Kim, K. J.; Zhu, Y.; Hood, Z. D.; Rupp, J. L. Processing thin but robust electrolytes for solid-state batteries. *Nat. Energy* **2021**, *6*, 227−239.
(11) Randau, S.; Weber, D. A.; Kötz, O.; Koerver, R.; Braun, P.; Weber, A.; Ivers-Tiffée, E.; Adermann, T.; Kulisch, J.; Zeier, W. G.; et al. Benchmarking the performance of all-solid-state lithium batteries. *Nat. Energy* **2020**, *5* (3), 259−270.
(12) Tan, D. H.; Banerjee, A.; Chen, Z.; Meng, Y. S. From nanoscale interface characterization to sustainable energy storage using all-solid-state batteries. *Nat. Nanotechnol.* **2020**, *15*, 170−180.
(13) Lee, Y.-G.; Fujiki, S.; Jung, C.; Suzuki, N.; Yashiro, N.; Omoda, R.; Ko, D.-S.; Shiratsuchi, T.; Sugimoto, T.; Ryu, S.; et al. High-energy long-cycling all-solid-state lithium metal batteries enabled by silver−carbon composite anodes. *Nat. Energy* **2020**, *5* (4), 299−308.
(14) Sakuda, A.; Kuratani, K.; Yamamoto, M.; Takahashi, M.; Takeuchi, T.; Kobayashi, H. All-solid-state battery electrode sheets prepared by a slurry coating process. *J. Electrochem. Soc.* **2017**, *164* (12), A2474.
(15) Tan, D. H.; Banerjee, A.; Deng, Z.; Wu, E. A.; Nguyen, H.; Doux, J.-M.; Wang, X.; Cheng, J.-h.; Ong, S. P.; Meng, Y. S.; Chen, Z. Enabling thin and flexible solid-state composite electrolytes by the scalable solution process. *ACS Appl. Energy Mater.* **2019**, *2* (9), 6542−6550.
(16) Self, E. C.; Hood, Z. D.; Brahmbhatt, T.; Delnick, F. M.; Meyer, H. M., III; Yang, G.; Rupp, J. L.; Nanda, J. Solvent-Mediated Synthesis of Amorphous Li_3PS_4/Polyethylene Oxide Composite Solid Electrolytes with High Li^+ Conductivity. *Chem. Mater.* **2020**, *32* (20), 8789−8797.
(17) Luo, S.; Wang, Z.; Fan, A.; Liu, X.; Wang, H.; Ma, W.; Zhu, L.; Zhang, X. A high energy and power all-solid-state lithium battery enabled by modified sulfide electrolyte film. *J. Power Sources* **2021**, *485*, 229325.
(18) Lee, K.; Kim, S.; Park, J.; Park, S. H.; Coskun, A.; Jung, D. S.; Cho, W.; Choi, J. W. Selection of binder and solvent for solution-processed all-solid-state battery. *J. Electrochem. Soc.* **2017**, *164* (9), A2075.
(19) Oh, D. Y.; Kim, D. H.; Jung, S. H.; Han, J.-G.; Choi, N.-S.; Jung, Y. S. Single-step wet-chemical fabrication of sheet-type electrodes from solid-electrolyte precursors for all-solid-state lithium-ion batteries. *J. Mater. Chem. A* **2017**, *5* (39), 20771−20779.
(20) Nam, Y. J.; Oh, D. Y.; Jung, S. H.; Jung, Y. S. Toward practical all-solid-state lithium-ion batteries with high energy density and safety: comparative study for electrodes fabricated by dry-and slurry-mixing processes. *J. Power Sources* **2018**, *375*, 93−101.
(21) Lee, J.; Lee, K.; Lee, T.; Kim, H.; Kim, K.; Cho, W.; Coskun, A.; Char, K.; Choi, J. W. In Situ Deprotection of Polymeric Binders for Solution-Processible Sulfide-Based All-Solid-State Batteries. *Adv. Mater.* **2020**, *32* (37), 2001702.
(22) Cunha, R. P.; Lombardo, T.; Primo, E. N.; Franco, A. A. Artificial Intelligence Investigation of NMC Cathode Manufacturing Parameters Interdependencies. *Batteries & Supercaps* **2020**, *3*, 60−67.
(23) Rucci, A.; Ngandjong, A. C.; Primo, E. N.; Maiza, M.; Franco, A. A. Tracking variabilities in the simulation of Lithium Ion Battery electrode fabrication and its impact on electrochemical performance. *Electrochim. Acta* **2019**, *312*, 168−178.
(24) Franco, A. A.; Rucci, A.; Brandell, D.; Frayret, C.; Gaberscek, M.; Jankowski, P.; Johansson, P. Boosting rechargeable batteries R&D by multiscale modeling: myth or reality? *Chem. Rev.* **2019**, *119* (7), 4569−4627.

(25) Ngandjong, A. C.; Rucci, A.; Maiza, M.; Shukla, G.; Vazquez-Arenas, J.; Franco, A. A. Multiscale simulation platform linking lithium ion battery electrode fabrication process with performance at the cell level. *J. Phys. Chem. Lett.* **2017**, *8* (23), 5966−5972.
(26) Thomitzek, M.; Schmidt, O.; Röder, F.; Krewer, U.; Herrmann, C.; Thiede, S. Simulating process-product interdependencies in battery production systems. *Procedia CIRP* **2018**, *72*, 346−351.
(27) Duquesnoy, M.; Lombardo, T.; Chouchane, M.; Primo, E. N.; Franco, A. A. Data-driven assessment of electrode calendering process by combining experimental results, in silico mesostructures generation and machine learning. *J. Power Sources* **2020**, *480*, 229103.
(28) Turetskyy, A.; Thiede, S.; Thomitzek, M.; von Drachenfels, N.; Pape, T.; Herrmann, C. Toward Data-Driven Applications in Lithium-Ion Battery Cell Manufacturing. *Energy Technol.* **2020**, *8* (2), 1900136.
(29) Bao, J.; Murugesan, V.; Kamp, C. J.; Shao, Y.; Yan, L.; Wang, W. Machine Learning Coupled Multi-Scale Modeling for Redox Flow Batteries. *Adv. Theory Simul.* **2020**, *3* (2), 1900167.
(30) Chen, C.; Zuo, Y.; Ye, W.; Li, X.; Deng, Z.; Ong, S. P. A critical review of machine learning of energy materials. *Adv. Energy Mater.* **2020**, *10* (8), 1903242.
(31) Severson, K. A.; Attia, P. M.; Jin, N.; Perkins, N.; Jiang, B.; Yang, Z.; Chen, M. H.; Aykol, M.; Herring, P. K.; Fraggedakis, D.; et al. Data-driven prediction of battery cycle life before capacity degradation. *Nat. Energy* **2019**, *4* (5), 383−391.
(32) Petrich, L.; Westhoff, D.; Feinauer, J.; Finegan, D. P.; Daemi, S. R.; Shearing, P. R.; Schmidt, V. Crack detection in lithium-ion cells using machine learning. *Comput. Mater. Sci.* **2017**, *136*, 297−305.
(33) Chemali, E.; Kollmeyer, P. J.; Preindl, M.; Emadi, A. State-of-charge estimation of Li-ion batteries using deep neural networks: A machine learning approach. *J. Power Sources* **2018**, *400*, 242−255.
(34) Shah, A.; Chauhan, Y.; Chaudhury, B. Principal component analysis based construction and evaluation of cryptocurrency index. *Expert Systems with Applications* **2021**, *163*, 113796.
(35) Likas, A.; Vlassis, N.; Verbeek, J. J. The global k-means clustering algorithm. *Pattern recognition* **2003**, *36* (2), 451−461.
(36) Hearst, M. A.; Dumais, S. T.; Osuna, E.; Platt, J.; Scholkopf, B. Support vector machines. *IEEE Intelligent Systems and their applications* **1998**, *13* (4), 18−28.
(37) McKight, P. E.; Najab, J. Kruskal-wallis test. *The Corsini Encyclopedia of Psychology* **2010**, DOI: 10.1002/9780470479216.corpsy0491.
(38) Churchill, G. A. Using ANOVA to analyze microarray data. *BioTechniques* **2004**, *37* (2), 173−177.
(39) Le, T.; Vo, M. T.; Vo, B.; Lee, M. Y.; Baik, S. W. A hybrid approach using oversampling technique and cost-sensitive learning for bankruptcy prediction. *Complexity* **2019**, *2019*, 8460934.
(40) Popović, M. chrF: character n-gram F-score for automatic MT evaluation. In *Proceedings of the Tenth Workshop on Statistical Machine Translation*, 2015; pp 392−395.
(41) Banerjee, A.; Wang, X.; Fang, C.; Wu, E. A.; Meng, Y. S. Interfaces and interphases in All-Solid-State batteries with inorganic solid electrolytes. *Chem. Rev.* **2020**, *120* (14), 6878−6933.
(42) Han, F.; Westover, A. S.; Yue, J.; Fan, X.; Wang, F.; Chi, M.; Leonard, D. N.; Dudney, N. J.; Wang, H.; Wang, C. High electronic conductivity as the origin of lithium dendrite formation within solid electrolytes. *Nat. Energy* **2019**, *4* (3), 187−196.
(43) Jung, S. H.; Kim, U. H.; Kim, J. H.; Jun, S.; Yoon, C. S.; Jung, Y. S.; Sun, Y. K. Ni-rich layered cathode materials with electrochemo-mechanically compliant microstructures for all-solid-state Li batteries. *Adv. Energy Mater.* **2020**, *10* (6), 1903360.
(44) Koerver, R.; Aygün, I.; Leichtweiß, T.; Dietrich, C.; Zhang, W.; Binder, J. O.; Hartmann, P.; Zeier, W. G.; Janek, J. r. Capacity fade in solid-state batteries: interphase formation and chemomechanical processes in nickel-rich layered oxide cathodes and lithium thiophosphate solid electrolytes. *Chem. Mater.* **2017**, *29* (13), 5574−5582.
(45) Zhang, W.; Schröder, D.; Arlt, T.; Manke, I.; Koerver, R.; Pinedo, R.; Weber, D. A.; Sann, J.; Zeier, W. G.; Janek, J. (Electro) chemical expansion during cycling: monitoring the pressure changes in operating solid-state lithium batteries. *J. Mater. Chem. A* **2017**, *5* (20), 9929−9936.
(46) Doux, J. M.; Nguyen, H.; Tan, D. H.; Banerjee, A.; Wang, X.; Wu, E. A.; Jo, C.; Yang, H.; Meng, Y. S. Stack Pressure Considerations for Room-Temperature All-Solid-State Lithium Metal Batteries. *Adv. Energy Mater.* **2020**, *10* (1), 1903253.
(47) Kasemchainan, J.; Zekoll, S.; Spencer Jolly, D.; Ning, Z.; Hartley, G.; Marrow, T.; Bruce, P. Critical stripping current leads to dendrite formation on plating in 3 lithium anode solid electrolyte cells. *Nat. Mater.* **2019**, *18* (10), 1105−1111.
(48) Doux, J.-M.; Yang, Y.; Tan, D. H.; Nguyen, H.; Wu, E. A.; Wang, X.; Banerjee, A.; Meng, Y. S. Pressure effects on sulfide electrolytes for all solid-state batteries. *J. Mater. Chem. A* **2020**, *8* (10), 5049−5055.
(49) Wang, Y.; Liu, T.; Kumar, J. Effect of Pressure on Lithium Metal Deposition and Stripping against Sulfide-Based Solid Electrolytes. *ACS Appl. Mater. Interfaces* **2020**, *12* (31), 34771−34776.